

# The Coronal Abundances of Mid-F Dwarfs

Brian E. Wood, J. Martin Laming

*Naval Research Laboratory, Space Science Division, Washington, DC 20375*

## ABSTRACT

A *Chandra* spectrum of the moderately active nearby F6 V star  $\pi^3$  Ori is used to study the coronal properties of mid-F dwarfs. We find that  $\pi^3$  Ori's coronal emission measure distribution is very similar to those of moderately active G and K dwarfs, with an emission measure peak near  $\log T = 6.6$  seeming to be ubiquitous for such stars. In contrast to coronal temperature, coronal abundances are known to depend on spectral type for main sequence stars. Based on this previously known relation, we expected  $\pi^3$  Ori's corona to exhibit an extremely strong "FIP effect," a phenomenon first identified on the Sun where elements with low "First Ionization Potential" (FIP) are enhanced in the corona. We instead find that  $\pi^3$  Ori's corona exhibits a FIP effect essentially identical to that of the Sun and other early G dwarfs, perhaps indicating that the increase in FIP bias towards earlier spectral types stops or at least slows for F stars. We find that  $\pi^3$  Ori's coronal characteristics are significantly different from two previously studied mid-F stars, Procyon (F5 IV-V) and  $\tau$  Boo (F7 V). We believe  $\pi^3$  Ori is more representative of the coronal characteristics of mid-F dwarfs, with Procyon being different because of luminosity class, and  $\tau$  Boo being different because of the effects of one of two close companions, one stellar ( $\tau$  Boo B: M2 V) and one planetary.

*Subject headings:* stars: individual ( $\pi^3$  Ori) — stars: coronae — stars: late-type — X-rays: stars

## 1. INTRODUCTION

Although details about stellar magnetic field generation remain uncertain, it is accepted that coronal magnetic fields are generated by a magnetic dynamo operating within the convection zone. For main sequence stars, the convection zone narrows towards earlier spectral types, disappearing entirely around a spectral type of A5 V. At this point, coronae disappear as well (Schmitt et al. 1985), emphasizing the central role that the convection zone dynamo plays in generating stellar coronae.

One general empirical goal of stellar coronal X-ray observations is to study how coronae change character as the convection zone narrows. Any clear correlation between coronal properties and spectral type tells us something useful about how the dynamo and the fields it generates change with spectral type, thereby providing potentially crucial information for theoretical models of how stellar magnetic dynamos operate in general.

Coronal abundances represent one coronal property that appears to be tightly correlated with spectral type, at least for main sequence stars. On the Sun, it has long been known that coronal abundances are different from photospheric abundances, elements with low First Ionization Potential (FIP) having enhanced abundances in the solar corona and solar wind (von Steiger et al. 1995; Feldman & Laming 2000). Analyses of X-ray and EUV spectra have found a similar “FIP effect” for some stars of low to moderate activity (Laming et al. 1996; Drake et al. 1997; Laming & Drake 1999; Telleschi et al. 2005). However, for many other stars, particularly extremely active ones, the FIP effect is either absent, or sometimes an inverse FIP effect is observed, where low-FIP elements have coronal abundances that are *depleted* relative to the high-FIP elements (Audard et al. 2001, 2003; Brinkman et al. 2001; Güdel et al. 2001; Huenemoerder et al. 2001, 2003; Sanz-Forcada et al. 2003, 2009; Ball et al. 2005; Liefke et al. 2008). Currently the only detailed theoretical model that is capable of explaining both solar-like FIP effects and inverse FIP effects is one that attributes the element fractionation to ponderomotive forces induced by Alfvén and other MHD waves passing through or reflecting from the chromosphere (Laming 2004, 2009, 2012; Wood et al. 2012).

Initially, it appeared that coronal abundances were primarily dependent on activity, as the most active stars clearly tend to have inverse FIP effects instead of a solar-like FIP effect. This activity dependence of abundances for active stars is illustrated and discussed in detail by Güdel (2004, see Figure 37). The abundance variations are not simply a uniform variation of low-FIP elements relative to high-FIP ones. The high-FIP elements appear to fractionate with respect to each other as well, as illustrated by measurements of Ne/O. The vast majority of spectroscopically observed stellar coronae exhibit high ratios of Ne/O  $\approx 0.4$  (Drake & Testa 2005), but relatively inactive stars (e.g., the Sun,  $\alpha$  Cen AB, and Procyon) show Ne/O  $\approx 0.2$  (Robrade et al. 2008).

As more abundance measurements have been made, it has become apparent that abundances are also highly dependent on spectral type (Güdel 2007; Güdel et al. 2007; Telleschi et al. 2007). In order to explore this further we have experimented with a high-FIP/low-FIP abundance ratio,  $F_{bias}$ , which quantifies a corona’s FIP bias as the average abundance of four high-FIP elements (C, N, O, and Ne) relative to Fe; normalized to photospheric abundance ratios. For normal main sequence stars with coronal X-ray luminosities of  $\log L_X < 29.1$  (in

ergs  $s^{-1}$ ), there is a surprisingly tight spectral type dependence for  $F_{bias}$  (Wood & Linsky 2010; Wood et al. 2012). In this correlation, early G stars all have a solar-like FIP effect, which decreases towards late G and early K stars, reaching no FIP effect at all at a spectral type of K5 V. Later than K5 V, inverse FIP effects are observed, with the magnitude of the effect increasing into the M dwarfs. We will refer to this as the “FIP-Bias/Spectral-Type” (FBST) relation. At least for stars with  $\log L_X < 29.1$ , any activity dependence for  $F_{bias}$  is lost in the scatter of the measurements.

The FBST relation would predict that the solar-like FIP effect should become even stronger as you move from solar-like early G stars to F stars. More precisely, instead of a factor of 4 enhancement of low FIP elements in the corona as for the Sun (Feldman & Laming 2000), the FBST relation would predict a factor of 6 enhancement for mid-F stars (Wood & Linsky 2010). However, observations of two mid-F dwarfs seem to contradict this expectation. The first of these is Procyon (F5 IV-V), the nearest and most frequently observed F star, which has been observed spectroscopically by EUVE, *Chandra*, and XMM. All of these spectra demonstrate that Procyon’s corona exhibits no significant FIP bias at all. Its coronal abundances are consistent with its photospheric abundances (Drake et al. 1995; Raassen et al. 2002). More recently, using XMM data Maggio et al. (2011) have also found little difference in the abundances of low-FIP and high-FIP elements in the corona of  $\tau$  Boo (F7 V), although they suggest that *both* are depleted in the corona by similar amounts.

The Procyon and  $\tau$  Boo measurements would seem to suggest that the FBST relation falls apart for the F dwarfs, possibly an effect of the thinning convection zones of such stars. This would be a very interesting result, but there are potential issues with both Procyon and  $\tau$  Boo regarding whether either can be considered representative of mid-F dwarfs. For Procyon, the problem is simply that it is not a pure main sequence star, as its “IV-V” luminosity class suggests. Its radius of  $2.05 R_{\odot}$  is certainly larger than that of a true mid-F main sequence star (Kervella et al. 2004).

For  $\tau$  Boo, the problem is the presence of two very different companions, one stellar and one planetary. The stellar companion,  $\tau$  Boo B, is an M2 V star that is unresolved from the primary in the XMM observation, which could in principle be contributing X-ray photons to the spectrum. Given that M dwarfs are expected to have inverse FIP effects (Wood et al. 2012), contamination from  $\tau$  Boo B would be expected to weaken any FIP effect in the combined X-ray spectrum. As for the planetary companion, it is a very well-studied close-in giant planet,  $\tau$  Boo b, with an orbital period of only 3.31 days. There is already evidence that the presence of this massive planet is producing coronal activity on the star (Shkolnik et al. 2008; Walker et al. 2008). Is it possible that the planet could somehow be suppressing the expected strong coronal FIP effect as well? This is an exciting possibility, which makes it

all the more important to know what the corona of a truly normal mid-F dwarf looks like.

To that end, we here present an analysis of recent *Chandra* observations of the nearby F6 V star,  $\pi^3$  Ori, which lies at a distance of 8.1 pc (Perryman et al. 1997). The star has a rapid rotation rate of  $v \sin i = 17.3 \text{ km s}^{-1}$ , corresponding to  $P_{rot}/\sin i = 4.1$  days (Ammler-von Eiff & Reiners 2012). Not surprisingly, given the known connection between stellar rotation and activity,  $\pi^3$  Ori also has a relatively high X-ray luminosity of  $\log L_X = 28.96$  (Schmitt & Liefke 2004), just barely within the  $\log L_X < 29.1$  activity regime mentioned above where the FBST relation remains tight. This is in fact one of the ten most luminous coronal X-ray sources within 10 pc, so it is curious that  $\pi^3$  Ori has never before been observed spectroscopically in X-rays. The  $\pi^3$  Ori spectrum promises to resolve the issue of what the coronal characteristics of moderately active mid-F main sequence stars really are.

## 2. DATA ANALYSIS

### 2.1. Observations of $\pi^3$ Ori

The *Chandra* X-ray telescope observed  $\pi^3$  Ori twice in late 2010, the first time on 2010 November 11 for 57.8 ksec, and a second time on 2010 November 23 for 20.1 ksec. The observations were performed with *Chandra*'s LETGS configuration, combining the Low Energy Transmission Grating (LETG) and the component of the High Resolution Camera detector used for spectroscopy (HRC-S).

The data were processed using version 4.3 of the *Chandra* team's CIAO software. The initial HRC-S image produced by the data processing consists of a zeroth-order image of the star, and an X-ray spectrum dispersed on both sides of the image, i.e., a plus and minus order spectrum. Further processing extracts one-dimensional spectra from the image, and then the plus and minus order spectra are coadded into a final spectrum covering the full 5 – 175 Å wavelength region of LETGS.

Photons in the time-tagged zeroth-order image are useful for assessing source variability. We find no significant variability at all for  $\pi^3$  Ori, and the X-ray fluxes appear to be identical at the two observing times, so we simply coadd the spectra taken at the two times into a final spectrum representing a combined exposure time of 77.9 ksec. This spectrum is shown in Figure 1.

## 2.2. Line Identification and Measurement

We use version 6.1 of the CHIANTI atomic database to identify emission lines in our spectrum (Dere et al. 1997, 2009). The identified lines are listed in Table 1, and identifications are also provided in Figure 1. Counts for the detected lines are measured by direct integration from the spectrum, and these raw counts are then converted to photon fluxes. Both the counts and fluxes of the lines are provided in Table 1, together with  $1\sigma$  uncertainties. The third column of the table lists line formation temperatures, based on ionization equilibrium computations from Arnaud & Rothenflug (1985).

There are many lines in Table 1 with large quoted uncertainties that represent questionable detections. The emission measure (EM) analysis described in section 2.3 is used to confirm *a posteriori* that these marginal detections are at least plausible. There are many line blends in Table 1. The EM analysis and the line strengths in the CHIANTI database are used to assess what lines are contributing significant flux to each emission feature. The line blends involving different species are ultimately ignored in the final EM analysis.

There are many density sensitive He-like triplets in the  $\pi^3$  Ori spectrum (Ness et al. 2002), but only the O VII triplet near 21.8 Å is sufficiently free of blends and with high enough signal-to-noise (S/N) for a decent density measurement. Unfortunately, even for O VII we find we can only quote an upper limit for the electron density. Based on the collisional equilibrium models of Porquet et al. (2001), the  $\lambda 22.101/\lambda 21.807$  line flux ratio corresponds to an electron density (in  $\text{cm}^{-3}$ ) of  $\log n_e < 10.70$ . Similarly low coronal densities have been found for many moderately active G and K dwarfs in the past (Wood & Linsky 2006, 2010), so there is no evidence that our moderately active F dwarf is any different from later type stars in terms of coronal density.

## 2.3. Emission Measure Analysis

Inferring coronal abundances and temperature distributions from line flux measurements requires an EM analysis, which is a nontrivial inversion problem. For this calculation, we use version 2.6 of the PINTofALE software package (Kashyap & Drake 1998, 2000), which was developed to solve the EM inversion problem using a Markov chain Monte Carlo approach. The analysis also makes use of CHIANTI line emissivities (Dere et al. 1997, 2009). Our EM analysis closely mirrors previous work, as described in particular detail by Wood & Linsky (2006), so we refer the reader to that paper for details about this computation.

The analysis considers the effects of interstellar absorption on the observed line fluxes. There is no measured H I column density towards  $\pi^3$  Ori itself, but there is a measurement

of  $\log N_H = 17.93$  (in  $\text{cm}^{-2}$ ) towards  $\chi^1$  Ori (Wood et al. 2005), which is roughly at the same distance and in the same direction as  $\pi^3$  Ori, so this is the value we assume. We note, however, that this value is low enough that interstellar absorption does not have a large effect on line fluxes.

The line fluxes by themselves allow the computation of the shape of the emission measure distribution, and the computation of relative coronal abundances. For the relative abundances, the natural reference element to use is Fe, considering the large number of Fe lines available in the LETGS spectrum. In the initial EM analysis we simply assume a solar photospheric abundance for our reference element,  $\log [\text{Fe}/\text{H}] = -4.50$  (Asplund et al. 2009). Table 2 lists the coronal abundances relative to Fe computed in the EM analysis, and Figure 2 shows the derived emission measure distribution. The 90% confidence intervals shown for the emission measures and abundances in Figure 2 and Table 2, respectively, are indicative of the uncertainties in solving the inversion problem, based on the magnitude of the uncertainties in the measured line fluxes.

Properly normalizing the EM distribution requires the measurement of an absolute coronal  $[\text{Fe}/\text{H}]$  ratio, which also allows the relative abundances in Table 2 to be converted to absolute abundances. Measurement of  $[\text{Fe}/\text{H}]$  requires an assessment of the line-to-continuum ratio in the LETGS spectrum, which can be done after the initial EM analysis is completed. Emission measures scale inversely with the assumed  $[\text{Fe}/\text{H}]$ , since higher metal abundances mean less emission measure is required to account for the line fluxes. Thus, increasing  $[\text{Fe}/\text{H}]$  by a factor of two from  $\log [\text{Fe}/\text{H}] = -4.50$  to  $\log [\text{Fe}/\text{H}] = -4.20$ , for example, uniformly lowers the EM distribution by a factor of two.

Synthetic line-plus-continuum spectra can be computed from the EM distribution for various values of  $[\text{Fe}/\text{H}]$  and compared with the data, in order to see which leads to the best match to the observed continuum level. This is illustrated in Figure 3, which shows the best fit for  $\log [\text{Fe}/\text{H}] = -4.32$ . This synthetic spectrum is also compared with the data in Figure 1. In LETGS data, higher order spectra are superimposed onto the first order spectrum, so the synthetic spectrum accounts for the higher order spectra as well, specifically orders 2–5. The higher order contributions are explicitly plotted in both Figures 1 and 3. The EM distribution in Figure 2 is the final normalized distribution assuming  $\log [\text{Fe}/\text{H}] = -4.32$ .

#### 2.4. The Shape of the Emission Measure Distribution

The most striking feature of the  $\pi^3$  Ori EM distribution in Figure 2 is a sharp peak at  $\log T = 6.6$ . This peak actually seems to be very common for moderately active stars

like  $\pi^3$  Ori. Many examples are provided by Wood & Linsky (2006, 2010), but the best of these are  $\xi$  Boo A (G8 V) and  $\epsilon$  Eri (K2 V). The EM distributions for these 2 stars are also shown in Figure 2. The  $\xi$  Boo A EM distribution is a particularly good match for that of  $\pi^3$  Ori. This is perhaps not surprising considering that  $\xi$  Boo A and  $\pi^3$  Ori have similar X-ray luminosities of  $\log L_X = 28.86$  and  $\log L_X = 28.96$ , respectively (Schmitt & Liefke 2004), although the spectral types of the two stars are quite different. Thus, there is no evidence that the thinner convection zone of  $\pi^3$  Ori has led to coronal temperatures any different from those of similarly active later type stars.

Interestingly enough, the  $\log T = 6.6$  peaks are also commonly observed for solar active regions (Warren et al. 2011, 2012). In Figure 2, the three stellar EM distributions are compared with a solar one, which represents the average of 15 active region EM distributions from Warren et al. (2012), who emphasized the prevalence of  $\log T = 6.6$  EM peaks on the Sun. The shape of the solar active region EM agrees beautifully with those of  $\pi^3$  Ori and  $\xi$  Boo A for  $\log T < 6.7$ , although the three stellar EM distributions in Figure 2 have much higher EM at  $\log T > 6.7$ . Drake et al. (2000) have previously noted the similarity between the EM distributions of solar active regions and those of  $\xi$  Boo A and  $\epsilon$  Eri, and have suggested that it implies that moderately active stars like these are covered almost completely with solar-like active regions.

Is it possible that these seemingly ubiquitous  $\log T = 6.6$  peaks are somehow a systematic artifact of the PINTofALE computations that produced them? Not only was PINTofALE’s Markov chain Monte Carlo approach used to compute the stellar EM distributions in Figure 2, but it was also used by Warren et al. (2011, 2012) to compute the solar ones. Note, however, that Warren et al. (2011, 2012) analyzed a completely different spectral region and a different set of emission lines than those used in the stellar analyses, suggesting that the  $\log T = 6.6$  peaks are not just a product of working with a particular set of lines. We explore this issue further using simulations. These simulations involve taking a known EM distribution, computing line fluxes from that distribution for the set of lines in Table 2, and then plugging those line fluxes back into PINTofALE to see if the EM inversion procedure can recover the original EM distribution. Uncertainties in the line fluxes are assumed to be the same as the relative uncertainties measured for the  $\pi^3$  Ori lines in Table 1. Some results of these simulations are shown in Figure 4.

The dotted line in Figure 4’s “Simulation 1” is simply the  $\pi^3$  Ori distribution from Figure 2. The solid line shows the result when that is used as the input EM distribution for the simulation. The computed EM distribution agrees encouragingly well with the original distribution, being within the displayed error bars for 15 of the 17 temperature bins. Most importantly, the simulation demonstrates PINTofALE’s ability to recover the sharp  $\log T =$

6.6 EM peak. In Simulations 2 and 3 we simply shift the peak to  $\log T = 6.5$  and  $\log T = 6.7$ , respectively, and in Simulation 4 we remove the peak entirely, assuming equal EM values in the  $\log T = 6.5 - 6.7$  range. Although the reconstructed EM values are still generally within error bars, we do note that for Simulations 2–4 the EM is systematically overpredicted at  $\log T = 6.6$  and underpredicted at  $\log T = 6.5$  and  $\log T = 6.7$ .

We conclude, therefore, that there may indeed be a modest tendency for PINTofALE to overemphasize the height and narrowness of the  $\log T = 6.6$  peaks, though the magnitude of this effect is not necessarily inconsistent with the inferred 90% confidence intervals. We can only speculate as to the source of this tendency. It does so happen that  $\log T = 6.6$  is the central formation temperature of the strongest lines in the LETGS spectrum, the Fe XVII lines between 15–17 Å, so perhaps the need to fit those line fluxes particularly well leads to the modest overemphasis of EM at  $\log T = 6.6$ , to the detriment of EM at  $\log T = 6.5$  and  $\log T = 6.7$ . In any case, despite evidence for this small systematic error, the simulations provide support for the existence of a distinct maximum of EM near  $\log T = 6.6$  for moderately active stars and solar active regions.

The question then becomes, why is  $\log T = 6.6$  such a popular temperature for both a variety of solar active regions, and for moderately active stars of various spectral types? Is there something special about this particular temperature? One notable thing about it is that there is a local minimum in the radiative cooling curve near  $\log T = 6.6$  (e.g., Colgan et al. 2008; Dudík et al. 2011). The cooling curve relates how emissivity varies with temperature. Plasma is stable against radiatively driven thermal instabilities where the cooling curve has a shallower slope than the temperature dependence of the heating function. The cooling curve has a steep negative slope for a variety of abundance sets in the range  $\log T = 6.1 - 6.5$ , which could imply thermal instability unless the heating curve has an even steeper negative slope at those temperatures. Thus,  $\log T = 6.6$  is possibly the coolest stable temperature above  $\log T = 6.1$ . Plasma initially between these two temperatures will most likely either heat up or cool down until a stable temperature is reached.

Perhaps the ubiquity of the  $\log T = 6.6$  peak implies something about the commonality of active region loops on the Sun and solar-like main sequence stars, consistent with the idea that coronal emission from moderately active stars like  $\pi^3$  Ori and  $\xi$  Boo A is dominated by solar-like active regions that largely cover the stellar surface (Drake et al. 2000). On the Sun, such loops are often found to have densities of  $n_e \sim 10^{10} \text{ cm}^{-3}$  (e.g., Winebarger et al. 2011). Such densities are consistent with those commonly measured in stellar coronae as well, at least at temperatures of  $\log T < 6.7$  (Ness et al. 2002; Wood & Linsky 2006, 2010). An explanation in terms of thermal stability presupposes that coronal plasma exists in structures (loops) that can support a quasi-steady state. No such explanation would be possible in

a corona heated and supplied by more dynamic phenomena such as Type II spicules (e.g., de Pontieu et al. 2011; McIntosh et al. 2011; Martínez-Sykora et al. 2011; Judge et al. 2012). In simple static loop models there is a relation between a coronal loop’s length and its apex temperature and density (Rosner et al. 1978; Vesecky et al. 1979; Jordan 1980; Reale 2010). Thus, if coronal loops in various solar and stellar contexts tend to have similar densities and lengths, then presumably they would have similar temperatures as well. This presumes, of course, that these simple static models apply, which is questionable (e.g., Lenz et al. 1999; Schmelz et al. 2009).

## 2.5. The Coronal Abundances of $\pi^3$ Ori

As discussed in section 2.3, the EM analysis provides coronal abundances measured relative to Fe for many elements. All of these measurements, in the form  $\log [X/Fe]$ , are listed in the second column of Table 2. We are interested in comparing coronal abundances with those of the photosphere. Thus, in the third column of Table 2, we list stellar photospheric abundance ratios relative to Fe, in the form  $\log [X/Fe]_*$ . The photospheric abundances of Allende Prieto et al. (2004) are measured using line-by-line comparisons of solar and stellar spectral features, so the abundance measurements are intrinsically relative to solar abundances. Thus, computing the stellar photospheric abundance ratios in Table 2 requires the assumption of solar abundances. The assumed solar abundances of Asplund et al. (2009) are listed in the last column of Table 2. For N and S, there are no stellar photospheric measurements available. We assume these elements behave like high-FIP elements, such as O. Thus, we assume  $\log [N_*/N_\odot] \equiv \log [S_*/S_\odot] \equiv \log [O_*/O_\odot] = 0.16$ .

Neon is a special case. The fundamental problem with Ne is that even for the Sun there is no real photospheric abundance measurement, because there are no solar photospheric Ne absorption lines. Reference solar abundances for Ne, such as the one listed in Table 2, are in reality based on measurements from the solar corona and transition region (e.g., Schmelz et al. 2005). We know very well that abundances can be different from photospheric in the corona, but not necessarily in the transition region, where Young (2005a,b) finds a low Ne/O abundance, and no evidence for a FIP effect in other elements. Nevertheless, we do know that high-FIP elements can be fractionated in the solar atmosphere, as He is depleted by a factor of 2 in the slow solar wind (von Steiger et al. 1995). This depletion of He (and also possibly of Ne) is also a feature of models for the solar FIP effect based on the ponderomotive force (Laming 2009, 2012; Rakowski & Laming 2012).

Complicating the issue further is the knowledge that moderately active and very active stars seem to universally have coronal Ne/O ratios much higher than that of the Sun and other

similarly inactive stars (Drake & Testa 2005; Wood & Linsky 2006; Robrade et al. 2008), raising the possibility that these stellar coronal Ne abundances may be a better measure of the true cosmic Ne abundance than the solar coronal Ne abundance usually referenced as such. We here follow the same convention as in our past papers and assume that the average stellar coronal Ne/O = 0.41 abundance ratio of Drake & Testa (2005) is indicative of the true cosmic abundance of Ne, and therefore applies to solar and stellar photospheres as well, including for  $\pi^3$  Ori. Thus, the  $\log [\text{Ne}/\text{Fe}]_*$  ratio in Table 2 is derived assuming Ne/O = 0.41, instead of the much lower solar ratio of Ne/O = 0.17. The validity of this assumption is very much debatable, but it does lead to coronal Ne abundances in better agreement with those of other high-FIP elements (see Figure 5).

After subtracting the logarithmic photospheric abundance ratios, the logarithmic coronal abundance ratios in Table 2 are in Figure 5a plotted versus FIP. The low-FIP elements are all roughly consistent with the reference low-FIP element, Fe. The high-FIP element abundances are lower by about  $-0.6$  dex, consistent with a FIP effect nearly identical to that of the Sun. The average value of the four high-FIP elements in Figure 5a is plotted explicitly as a horizontal dot-dashed line in the figure. This is the “FIP bias” quantity,  $F_{bias}$ , that we have used in the past to reduce coronal abundances to a single number, which is then used to study the FBST relation described in section 1 (Wood & Linsky 2010; Wood et al. 2012). For  $\pi^3$  Ori,  $F_{bias} = -0.55$ .

The  $F_{bias}$  quantity has no clear variation with activity for main sequence stars with  $\log L_X < 29.1$  (see Figure 4 in Wood et al. 2012), but it is worth noting that of the four high-FIP elements that go into computing  $F_{bias}$  (C, N, O, and Ne), Ne is once again an exception, as we know that the coronal Ne/O ratio does vary within the  $\log L_X < 29.1$  sample, suggesting activity-dependent fractionation of Ne even for less active stars (Robrade et al. 2008). As alluded to above, the vast majority of spectroscopically observed  $\log L_X < 29.1$  stars, including  $\pi^3$  Ori, have Ne/O  $\approx 0.4$ . Only a few truly inactive stars (the Sun and  $\alpha$  Cen AB) have Ne/O  $\approx 0.2$  (Wood et al. 2012).

There are a couple characteristics of the low-FIP elements that are worthy of note. Maggio et al. (2011) found that the coronal Ni abundance of the mid-F dwarf  $\tau$  Boo was anomalously high compared to other low-FIP elements, being a factor of 2 – 3 higher. We do not see this behavior for our mid-F dwarf,  $\pi^3$  Ori. The Ni abundance may be a little high in Figure 5, but it is consistent with the other low-FIP elements within the error bars. As for Mg and Si, in the past we had noted a tendency for Mg abundances to be higher than Si abundances in the coronae of many moderately active stars (Wood & Linsky 2010). This is not the case for  $\pi^3$  Ori, though, which if anything shows the opposite behavior, consistent with what Maggio et al. (2011) found for  $\tau$  Boo.

Figure 5a shows the coronal abundance measurements relative to Fe. But using the  $\log [\text{Fe}/\text{H}] = -4.32$  measurement from the line-to-continuum analysis, we can compute absolute abundances as well, and in Figure 5b the absolute abundances are plotted, relative to stellar photospheric abundances as before. This figure casts doubt on whether the coronal abundance fractionation pattern of  $\pi^3$  Ori is truly solar-like or not.

Based on Figure 5a, the  $\pi^3$  Ori coronal abundances were described above as very solar-like, because the  $F_{bias} = -0.55$  measurement implies a factor of 4 underabundance of high-FIP elements relative to low-FIP elements in the corona, similar to the situation in the solar corona. But in the solar corona this is really due to an enhancement of low-FIP elements, as opposed to a depletion of high-FIP elements, meaning that for the Sun the high-FIP elements would be near 0.0 in Figure 5b and the low-FIP elements would be near 0.6. In contrast, Figure 5b would imply that for  $\pi^3$  Ori, the  $F_{bias} = -0.55$  result is due to fractionation of *both* low-FIP and high-FIP elements, and is in fact mostly due to a depletion of high-FIP elements.

This is actually consistent with what we have found before for other moderately active stars (Wood & Linsky 2006). The question is whether this means that the fractionation behavior of these stars really is significantly different from the Sun, or whether there is a systematic error in the line-to-continuum analysis that leads to systematic underestimates of  $\log [\text{Fe}/\text{H}]$ . The history of solar coronal abundance measurements provides reason for caution with regards to the accuracy of the line-to-continuum analysis, as many such solar analyses have found the data more consistent with a high-FIP depletion than a low-FIP enhancement (Veck & Parkinson 1981; Fludra & Schmelz 1995), contradicting other evidence, including direct solar wind measurements, that suggest low-FIP enhancement is the primary effect (von Steiger et al. 1995; Feldman & Laming 2000).

One concern is the possible presence of weak metal lines not listed in atomic line databases. These lines could collectively produce a significant pseudo-continuum in X-ray spectra, leading to overestimates of the strength of the real continuum, corresponding to an underestimate of  $\log [\text{Fe}/\text{H}]$ . There is hope that modern databases such as CHIANTI with more extensive line lists have greatly reduced this problem, but it is difficult to quantify what the systematic uncertainties really are. Another potential issue is the effect of non-Maxwellian distributions on the line-to-continuum analysis. Non-Maxwellian distributions will affect the analysis of both the line and continuum fluxes, but in different ways (Dudík et al. 2011, 2012).

All these issues provide justification for relying primarily on relative, rather than absolute abundances. The latter introduces the uncertain systematic errors involved in the line-to-continuum analysis, while the former does not. Nevertheless, when using relative

abundances, and quantities derived from them such as  $F_{bias}$ , it is important to keep in mind that the issue of absolute abundances has been left unresolved. A negative  $F_{bias}$  value, for example, could indicate either a low-FIP enhancement or a high-FIP depletion, and two stars with identical  $F_{bias}$  values could in principle be different in that respect. That being said, it is hard to imagine how the rather tight FBST relation shown in Figure 6 (and discussed in detail in the next section) could exist without some consistency regarding how  $F_{bias}$  relates to absolute abundances. For example, the FBST relation suggests M4 V stars all have  $F_{bias} \approx 0.45$  (Wood et al. 2012). It is hard to imagine why these stars would have different degrees of low-FIP depletions and/or high-FIP enhancements, but always calibrated so that  $F_{bias} \approx 0.45$ .

### 3. REASSESSING THE CORONAL ABUNDANCE PROBLEM

#### 3.1. $\pi^3$ Ori and the FBST Relation

As described in section 1, one of the main goals of the  $\pi^3$  Ori analysis is to see whether the FBST relation extends to F spectral types. The answer is provided in Figure 6. A full list of the stars plotted in the figure is provided by Wood et al. (2012), but we now add the  $\pi^3$  Ori data point.

Based on the G, K, and M stars in the figure,  $\pi^3$  Ori would be expected to have  $F_{bias} \approx -0.8$ , potentially the strongest solar-like FIP effect ever observed. Instead it has  $F_{bias} = -0.55$ , comparable to the Sun and other early G stars. There are three possible interpretations for the higher-than-expected  $F_{bias}$  measurement for  $\pi^3$  Ori:

1. Simply taken at face value, the  $\pi^3$  Ori measurement indicates that the FBST relation flattens towards spectral types earlier than G. Observations of early F dwarfs would be very useful to verify this flattening. If real, the flattening of the FBST relation could be interpreted as an interesting manifestation of the narrowing convection zone.
2. Although somewhat higher than expected, it could be argued that the  $\pi^3$  Ori measurement is still close enough to the expected  $F_{bias} \approx -0.8$  value to be considered consistent with a near-linear FBST relation, considering the amount of scatter that one sees in Figure 6.
3. Perhaps  $\pi^3$  Ori is actually too active to precisely follow the FBST relation. It is known that stars with  $\log L_X > 29.1$  lie significantly above the FBST relation (Wood et al. 2012). With  $\log L_X = 28.96$  (Schmitt & Liefke 2004),  $\pi^3$  Ori is close to this limit. If

the  $L_X$  limit is actually spectral type dependent, and lower for F dwarfs,  $\pi^3$  Ori would be expected to lie somewhat above the FBST curve.

In section 1, there were two F dwarfs discussed that are known from previously published work to be inconsistent with the FBST relation: Procyon (F5 IV-V) and  $\tau$  Boo (F7 V). Based on measurements from Raassen et al. (2002) and Maggio et al. (2011), we compute values of  $F_{bias} = 0.12$  and  $F_{bias} = -0.17$  for Procyon and  $\tau$  Boo, respectively. These values are plotted in Figure 6, explicitly showing just how inconsistent these two stars are with both  $\pi^3$  Ori and the FBST relation.

As for Procyon, the problem is that it is not a pure main sequence star, as its “IV-V” luminosity class and large  $2.05 R_\odot$  radius demonstrate (Kervella et al. 2004). Not only does Procyon have coronal abundances very different from  $\pi^3$  Ori, but it has a much cooler corona as well, with an EM peak near  $\log T = 6.2$  and no significant EM above  $\log T = 6.4$  (Raassen et al. 2002). Cool coronae are associated with less active stars, but Procyon’s X-ray luminosity is  $\log L_X = 28.51$ , only a factor of 3 lower than  $\pi^3$  Ori, and comparable to many of the stars in the Figure 6 sample with hotter coronae. For example,  $\epsilon$  Eri has a coronal X-ray luminosity of  $\log L_X = 28.33$  (Schmitt & Liefke 2004), lower than Procyon, but it has an EM distribution similar to  $\pi^3$  Ori (see Figure 2). We believe that Procyon’s inconsistency with  $\pi^3$  Ori emphasizes just how sensitive coronal properties can be to luminosity class. Procyon simply cannot be considered to be a main sequence star, and it is dramatically inconsistent with the FBST relation as a consequence.

As for  $\tau$  Boo, the inconsistency of  $\tau$  Boo with  $\pi^3$  Ori strengthens the argument made in section 1 that  $\tau$  Boo’s high  $F_{bias}$  value is due to one of its two companions. Either the M2 V companion,  $\tau$  Boo B, is contributing substantial flux to the XMM exposure, leading to erroneous abundance measurements, or the close-in giant planet,  $\tau$  Boo b, is somehow affecting the coronal abundances. The latter possibility is easily the more interesting of the two, as it would add a new twist to the current hot topic of star-planet interaction.

### 3.2. What Determines Coronal Abundances?

At this point it is worthwhile to summarize what we know about how coronal abundances depend on stellar properties. The stellar properties that we know affect  $F_{bias}$  are:

1. Spectral Type. This is the FBST relation illustrated in Figure 6. There are numerous basic stellar, photospheric, and convection zone properties that are known to be tightly correlated with spectral type for main sequence stars (stellar radius, temperature,

mass, surface gravity, convection zone depth, etc.). The existence of the FBST relation demonstrates that somehow one or more of these characteristics also determines coronal abundances. It is worth noting that a spectral type dependence is also known to exist for T Tauri stars and very active main sequence stars (Güdel et al. 2007; Wood et al. 2012).

2. Activity and/or Rapid Rotation. The FBST relation seems to work very well for the vast majority of main sequence stars. However, there is clearly an activity dependence as well. This is most evident for extremely active stars with  $\log L_X > 29.1$ , which all lie significantly above the FBST relation in Figure 6 (Wood et al. 2012). This activity dependence is also clearly seen in Figure 37 of Güdel (2004). An indication that activity dependence of coronal abundances extends to less active stars is the difference in Ne/O seen between moderately active stars and truly inactive stars like the Sun (Robrade et al. 2008). For the activity extremes, it is possible that some aspect of high activity (e.g., high magnetic field strength) is affecting coronal abundances. But it is also possible that the underlying cause of the extreme activity, rapid rotation, is the true determining factor. Perhaps very rapid rotation affects photospheric and/or convection zone characteristics, thereby allowing coronal abundances to be altered in the same manner as spectral type affects abundances in the FBST relation.
3. Luminosity Class. The best example of this is the  $\pi^3$  Ori/Procyon dichotomy discussed in section 3.1. There are evolved stars other than Procyon that would lie above the FBST relation in Figure 6, but most are part of active binaries (Brinkman et al. 2001; Huenemoerder et al. 2001; Audard et al. 2001, 2003). For such stars, it is not clear whether the discrepancy from the FBST relation is truly due to luminosity class, or whether it is instead an effect of high activity or in some cases particularly close binarity.

Is there a common theme that can be found among these abundance determinants? One avenue to explore concerns photospheric oscillation properties, which are known to depend on both spectral type and luminosity class (#1 and #3 above), and may depend on rotation and activity as well (#2). If coronal abundance fractionation is controlled by Alfvén and other MHD waves traveling through the chromosphere, as suggested by Laming (2004, 2009, 2012), the photospheric oscillation characteristics might be expected to be crucial, since these oscillations are likely sources of many of the chromospheric waves.

Oscillation frequencies increase and amplitudes decrease towards later type stars on the main sequence (Kjeldsen & Bedding 1995, 2011; Chaplin et al. 2008), which have higher  $F_{bias}$  values. This would imply a potential connection between high  $F_{bias}$  and oscillations

with high frequency and/or low amplitude. Unfortunately, this hypothetical connection is not consistent with the  $\pi^3$  Ori/Procyon dichotomy. Oscillation frequencies decrease and amplitudes increase as stars evolve off the main sequence (Kjeldsen & Bedding 1995, 2011; Chaplin et al. 2008), so the aforementioned main sequence oscillation/ $F_{bias}$  connection would predict *lower*  $F_{bias}$  for Procyon compared with  $\pi^3$  Ori. This is inconsistent with what we observe, so photospheric oscillation properties cannot be the sole determinant of coronal abundances.

### 3.3. A Possible Theoretical Framework for Resolving the Coronal Abundance Problem

Turning to theoretical considerations, we outline a framework for trying to interpret the observed coronal abundance variations in solar-like stars. Laming (2009, 2012) and Rakowski & Laming (2012) argue that the Alfvén waves giving rise to the ponderomotive force that generates the solar FIP effect most plausibly have a coronal origin. This is because waves in resonance with a coronal loop having period  $\tau = 2L/nv_A$ , where  $L$  is the coronal loop length and  $v_A$  is the coronal Alfvén speed, are required to produce the observed coronal depletion of He, and the only way to guarantee such a matching is if processes in the corona (e.g., nanoflares) excite normal modes of the loop. Wood et al. (2012) present a “toy model” of the inverse FIP effect, where fast mode waves propagating up through the chromosphere from below are reflected back down again in the region of the chromosphere where the Alfvén speed is increasing with height. This wave population gives a ponderomotive force directed *downwards*, which competes with the *upwards* ponderomotive force induced by the coronal Alfvén waves propagating downwards and reflecting back up. We argue that at the F and G dwarf end of the FBST relation, the positive FIP effect from coronal Alfvén waves dominates, while at the M dwarf end the inverse FIP effect due to initially upward propagating fast mode waves dominates, with a transition between the two somewhere in the K dwarfs.

Why should this be so? We discuss first the coronal Alfvén waves. These are assumed to arise from coronal nanoflare reconnection events. Several authors (e.g., Longcope & Tarr 2012; Kigure et al. 2010; Sturrock 1999) have argued that at least some, and maybe even most, of the magnetic energy released in reconnection should be converted to kinetic energy or waves in the surrounding plasma. It is plausible that such wave generation explains why surveys to find localized hot plasma as evidence of nanoflare reconnection have generally been unsuccessful (e.g., Warren et al. 2011). Instead, energy goes from magnetic field to waves, and is thus gradually dissipated as heat throughout the corona, and not quickly and locally as might have been expected.

Drake et al. (2006) studied the efficiency of electron acceleration in reconnection with the ambient plasma  $\beta$  (the electron plasma  $\beta_e = 8\pi n_e k_B T_e / B^2$ , to be more precise). They found maximum energy input to electrons at  $\beta_e = 0$ , with reduced electron heating at higher  $\beta_e$ , or lower magnetic field. We suggest that at the left hand side of the FBST relation, coronal reconnection primarily generates Alfvén waves that end up causing positive FIP fractionation when they reflect from the chromosphere. As one moves to the right, to later spectral type, coronal reconnection puts more energy into electrons, and less into waves. Consequently, the positive FIP effect diminishes.

Conversely, it is also possible that the amplitudes of fast mode waves penetrating the chromosphere from below and reflecting back down again may increase toward later spectral types, thus increasing the inverse FIP effect. Even though p-mode amplitudes decrease towards later type stars (Kjeldsen & Bedding 1995, 2011; Chaplin et al. 2008), it is possible that later type stars could be more efficient at converting the p-mode oscillations to fast mode MHD waves. Different regions of the Sun are different in this respect. It is known that sunspots are sinks of p-mode energy (see Braun 1995, and references therein), most likely through mode conversion or resonant absorption to Alfvén or fast mode waves. There are many cases of sunspots, active regions, and flares observed to have reduced FIP effects (e.g. Feldman et al. 1990; Phillips et al. 1994, 2006), although it is useful to note that an inverse FIP effect has never been reported in any solar observation.

An important factor that could act to restrict inverse FIP effects to later spectral types is the expansion of the magnetic field within the chromosphere. In their “toy model,” Wood et al. (2012) found that the density and magnetic field scale heights,  $H_D$  and  $H_B$ , were required to satisfy  $|H_D| < |H_B|/6$  to yield an inverse FIP effect. Although more realistic models are required to refine this relation, we note that  $H_D$  should be smaller for later spectral types due to higher surface gravities, allowing the relation to be met more readily if  $H_B$  does not also systematically decrease with spectral type. It is also worth noting that this relation will be met more readily for extremely active stars with magnetic fields so crowded that the fields cannot expand in the chromosphere, which effectively means an increase in  $H_B$ . This could potentially explain the tendency towards high  $F_{bias}$  for extremely active stars (dependence #2 in section 3.2).

The  $\pi^3$  Ori/Procyon dichotomy (see section 3.1) remains difficult to explain within this framework. Procyon would have larger  $H_D$  than  $\pi^3$  Ori, which would bias the star towards lower  $F_{bias}$ , not higher (as observed), assuming magnetic field expansion is the central issue. If  $H_B$  increases by much more than  $H_D$  as one moves from the main sequence to more evolved stars, that would reverse this behavior, but we know of no physical reason to expect this to be the case.

Perhaps Procyon has a fundamentally different coronal heating mechanism than the stars that follow the FBST relation. We have argued in section 2.4 that the commonly observed emission measure spike at  $\log T \simeq 6.6$  would be inconsistent with a Type II spicule model of coronal heating and mass supply, if interpreted in terms of a thermal stability argument. But Procyon does not possess this peak (see section 3.1), so a spicule-based coronal heating picture might work for Procyon. Such a model could also be consistent with Procyon’s lack of a FIP effect, because the spicule flow speed up through the chromosphere would conceivably be too fast to allow fractionation to occur. In this picture, the lower surface gravity of Procyon would allow upward propagating spicules to reach higher altitude and presumably higher temperature than on main sequence stars, potentially allowing the spicules to dominate the rather cool coronal emission observed from the star. Drake et al. (1995, their subsection 6.2) previously argued that the absence of FIP effect in the corona of Procyon is due to the effect of “unresolved fine structures” extending to higher temperatures there than they do on the Sun.

These speculations provide a framework for trying to understand how coronal abundances depend on stellar parameters. We hope this discussion can serve to focus attention on the critical observational and theoretical points required to subject it to further scrutiny.

We would like to thank Harry Warren for providing us with the solar active region EM distribution in Figure 2, and the referee Manuel Güdel for helpful comments. Support for this work was provided by NASA through ATP award NNH11AQ23I and Chandra Award Number GO1-12012Z issued by the Chandra X-ray Center (CXC).

## REFERENCES

- Allende Prieto, C., Barklem, P. S., Lambert, D. L., & Cunha, K. 2004, *A&A*, 420, 183
- Ammler-von Eiff, M., & Reiners, A. 2012, *A&A*, 542, A116
- Arnaud, M., & Rothenflug, R. 1985, *A&AS*, 60, 425
- Asplund, M., Grevesse, N., Sauval, A. J., & Scott, P. 2009, *ARA&A*, 47, 481.
- Audard, M., Behar, E., Güdel, M., Raassen, A. J. J., Porquet, D., Mewe, R., Foley, C. R., & Bromage, G. E. 2001, *A&A*, 365, L329
- Audard, M., Güdel, M., Sres, A., Raassen, A. J. J., & Mewe, R. 2003, *A&A*, 398, 1137

- Ball, B., Drake, J. J., Lin, L., Kashyap, V., Laming, J. M., & García-Alvarez, D. 2005, *ApJ*, 634, 1336
- Braun, D. C. 1995, *ApJ*, 451, 859
- Brinkman, A. C., et al. 2001, *A&A*, 365, L324
- Chaplin, W. J., Houdek, G., Appourchaux, T., Elsworth, Y., New, R., & Toutain, T. 2008, *A&A*, 485, 813
- Chaplin, W. J., Elsworth, Y., Isaak, G. R., Miller, B. A., & New, R. 2000, *MNRAS*, 313, 32
- Colgan, J., Abdullah, J. Jr., Sherrill, M. E., Foster, M., Fontes, C. J., & Feldman, U. 2008, *ApJ*, 689, 585
- de Pontieu, B., et al. 2011, *Science*, 33, 55
- Dere, K. P., Landi, E., Mason, H. E., Monsignori Fossi, B. C., & Young, P. R. 1997, *A&AS*, 125, 149
- Dere, K. P., Landi, E., Young, P. R., Del Zanna, G., Landini, M., & Mason, H. E. 2009, *A&A*, 498, 915
- Drake, J. F., Swisdak, M., Che, H., & Shay, M. A. 2006, *Nature*, 443, 553
- Drake, J. J., Laming, J. M., & Widing, K. G. 1995, *ApJ*, 443, 393
- Drake, J. J., Laming, J. M., & Widing, K. G. 1997, *ApJ*, 478, 403
- Drake, J. J., Peres, G., Orlando, S., Laming, J. M., & Maggio, A. 2000, *ApJ*, 545, 1074
- Drake, J. J., & Testa, P. 2005, *Nature*, 436, 525
- Dudík, J., Dzifčáková, E., Karlický, M., & Kulinová, A. 2011, *A&A*, 529, A103
- Dudík, J., Kašparová, J., Dzifčáková, E., Karlický, M., & Mackovjak, Š. 2012, *A&A*, 539, A107
- Feldman, U., & Laming, J. M. 2000, *Phys. Scr.*, 61, 222
- Feldman, U., Widing, K. G., & Lund, P. A. 1990, *ApJ*, 364, L21
- Fludra, A., & Schmelz, J. T. 1995, *ApJ*, 447, 936
- Güdel, M. 2004, *A&AR*, 12, 71

- Güdel, M. 2007, *Living Rev. Sol. Phys.*, 4, 3 (<http://www.livingreviews.org/lrsp-2007-3>)
- Güdel, M., et al. 2001, *A&A*, 365, L336
- Güdel, M., Skinner, S. L., Mel'nikov, S. Y., Audard, M., Telleschi, A., & Briggs, K. R. 2007, *A&A*, 468, 529
- Huenemoerder, D. P., Canizares, C. R., Drake, J. J., & Sanz-Forcada, J. 2003, *ApJ*, 595, 1131
- Huenemoerder, D. P., Canizares, C. R., & Schulz, N. S. 2001, *ApJ*, 559, 1135
- Jordan, C. 1980, *A&A*, 86, 355
- Judge, P. G., de Pontieu, B., McIntosh, S. W., & Kosovare, O. 2012, *ApJ*, 746, 158
- Kashyap, V. & Drake, J. J. 1998, *ApJ*, 503, 450
- Kashyap, V., & Drake, J. J. 2000, *Bull. Astron. Soc. India*, 28, 475
- Kervella, P., Thévenin, F., Morel, P., Berthomieu, G., Bordé, P., & Provost, J. 2004, *A&A*, 413, 251
- Kigure, H., Takahashi, K., Shibata, K., Yokoyama, T., & Nozawa, S. 2010, *PASJ*, 62, 993
- Kjeldsen, H., & Bedding, T. R. 1995, *A&A*, 293, 87
- Kjeldsen, H., & Bedding, T. R. 2011, *A&A*, 529, L8
- Laming, J. M. 2004, *ApJ*, 614, 1063
- Laming, J. M. 2009, *ApJ*, 695, 954
- Laming, J. M. 2012, *ApJ*, 744, 115
- Laming, J. M., & Drake, J. J. 1999, *ApJ*, 516, 324
- Laming, J. M., Drake, J. J., & Widing, K. G. 1996, *ApJ*, 462, 948
- Laming, J. M., Drake, J. J., & Widing, K. G. 1995, *ApJ*, 443, 416
- Lenz, D. D., DeLuca, E. E., Golub, L., Rosner, R., & Bookbinder, J. A. 1999, *ApJ*, 517, L155
- Liefke, C., Ness, J. -U., Schmitt, J. H. M. M., & Maggio, A. 2008, *A&A*, 491, 859

- Longcope, D. W., & Tarr, L. 2012, *ApJ*, 756, 192
- Maggio, A., Sanz-Forcada, J., & Scelsi, L. 2011, *A&A*, 527, A144
- Martínez-Sykora, J., Hansteen, V., & Moreno-Insertis, F. 2011, *ApJ*, 736, 9
- McIntosh, S. W., de Pontieu, B., Carlsson, M., Hansteen, V., Boerner, P., & Goossens, M. 2011, *Nature*, 475, 477
- Ness, J. -U., Schmitt, J. H. M. M., Burwitz, V., Mewe, R., Raassen, A. J. J., van der Meer, R. L. J., Predehl, P., & Brinkman, A. C. 2002, *A&A*, 394, 911
- Perryman, M. A. C., et al. 1997, *A&A*, 323, L49
- Phillips, K. J. H., Chifor, C., & Dennis, B. R. 2006, *ApJ*, 647, 1480
- Phillips, K. J. H., Pike, C. D., Lang, J., Watanabe, T., & Takahashi, M. 1994, *ApJ*, 435, 888
- Porquet, D., Mewe, R., Dubau, J., Raassen, A. J. J., & Kaastra, J. S. 2001, *A&A*, 376, 1113
- Raassen, A. J. J., et al. 2002, *A&A*, 389, 228
- Rakowski, C. E., & Laming, J. M. 2012, *ApJ*, 754, 65
- Reale, F. 2010, *Living Rev. Solar Phys.*, 7, 5, URL: <http://www.livingreviews.org/lrsp-2010-5>
- Robrade, J., Schmitt, J. H. M. M., & Favata, F. 2008, *A&A*, 486, 995
- Rosner, R., Tucker, W. H., & Vaiana, G. S. 1978, *ApJ*, 220, 643
- Sanz-Forcada, J., Affer, L., & Micela, G. 2009, *A&A*, 505, 299
- Sanz-Forcada, J., Maggio, A., & Micela, G. 2003, *A&A*, 408, 1087
- Schmelz, J. T., Nasraoui, K., Rightmire, L. A., Kimble, J. A., del Zanna, G., Cirtain, J. W., DeLuca, E. E., & Mason, H. E. 2009, *ApJ*, 691, 503
- Schmelz, J. T., Nasraoui, K., Roames, J. K., Lippner, L. A., & Garst, J. W. 2005, *ApJ*, 634, L197
- Schmitt, J. H. M. M., Golub, L., Harnden, F. R., Jr., Maxson, C. W., Rosner, R., & Vaiana, G. S. 1985, *ApJ*, 290, 307
- Schmitt, J. H. M. M., & Liefke, C. 2004, *A&A*, 417, 651

- Shkolnik, E., Bohlender, D. A., Walker, G. A. H., & Collier Cameron, A. 2008, *ApJ*, 676, 628
- Simoniello, R., Finsterle, W., García, R. A., Salabert, D., Jiménez, A., Elsworth, Y., & Schunker, H. 2010, *A&A*, 516, A30
- Sturrock, P. A. 1999, *ApJ*, 521, 451
- Telleschi, A., Güdel, M., Briggs, K., Audard, M., Ness, J. -U., & Skinner, S. L. 2005, *ApJ*, 622, 653
- Telleschi, A., Güdel, M., Briggs, K. R., Audard, M., & Scelsi, L. 2007, *A&A*, 468, 443
- Veck, N. J., & Parkinson, J. H. 1981, *MNRAS*, 197, 41
- Vesecky, J. F., Antiochos, S. K., & Underwood, J. H. 1979, *ApJ*, 233, 987
- von Steiger, R., Wimmer-Schweingruber, R. F., Geiss, J., & Gloeckler, G. 1995, *Adv. Space Res.*, 15(7), 3
- Walker, G. A. H., et al. 2008, *A&A*, 482, 691
- Warren, H. P., Brooks, D. H., & Winebarger, A. R. 2011, *ApJ*, 734, 90
- Warren, H. P., Winebarger, A. R., & Brooks, D. H. 2012, *ApJ*, 759, 141
- Winebarger, A. R., Schmelz, J. T., Warren, H. P., Saar, S. H., & Kashyap, V. L. 2011, *ApJ*, 740, 2
- Wood, B. E., Laming, J. L., & Karovska, M. 2012, *ApJ*, 753, 76
- Wood, B. E., & Linsky, J. L. 2006, *ApJ*, 643, 444
- Wood, B. E., & Linsky, J. L. 2010, *ApJ*, 717, 1279
- Wood, B. E., Redfield, S., Linsky, J. L., Müller, H. -R., & Zank, G. P. 2005, *ApJS*, 159, 118
- Young, P. R. 2005a, *A&A*, 439, 361
- Young, P. R. 2005b, *A&A*, 444, L45

Table 1. *Chandra* Line Measurements

Ion	$\lambda_{rest}$ (Å)	$\log T$	Counts	Flux ( $10^{-5}$ cm $^{-2}$ s $^{-1}$ )
Si XIII	6.648	6.99	142.0 ± 30.3	4.14 ± 0.88
Si XIII	6.688	6.99		
Si XIII	6.740	6.99		
Mg XII	8.419	7.11	56.9 ± 20.2	1.97 ± 0.70
Mg XII	8.425	7.11		
Mg XI	9.169	6.80	164.2 ± 27.3	6.63 ± 1.10
Mg XI	9.231	6.80		
Mg XI	9.314	6.79		
Ne X	12.132	6.87	191.7 ± 23.8	8.89 ± 1.10
Ne X	12.138	6.87		
Fe XVII	12.264	6.62	117.3 ± 21.4	5.47 ± 1.00
Fe XXI	12.285	6.98		
Ni XIX	12.435	6.69	74.2 ± 20.1	3.48 ± 0.94
Ne IX	13.447	6.58	314.3 ± 36.4	14.41 ± 1.67
Ne IX	13.553	6.58		
Ne IX	13.699	6.58	98.2 ± 22.9	4.51 ± 1.05
Fe XVII	13.823	6.60	173.2 ± 27.4	7.97 ± 1.26
Ni XIX	14.043	6.68	39.1 ± 18.9	1.80 ± 0.87
Ni XIX	14.077	6.68		
Fe XVIII	14.203	6.74	292.1 ± 33.8	13.47 ± 1.56
Fe XVIII	14.208	6.74		
Fe XVII	15.015	6.59	990.1 ± 44.4	44.83 ± 2.01
Fe XVII	15.262	6.59	481.6 ± 34.7	21.66 ± 1.56
O VIII	15.176	6.65		
Fe XIX	15.298	6.83		
O VIII	16.006	6.63	432.2 ± 34.2	19.77 ± 1.56
Fe XVIII	16.005	6.73		
Fe XVIII	16.072	6.73		
Fe XVII	16.778	6.58	650.1 ± 36.4	29.20 ± 1.63
Fe XVII	17.053	6.58	1428.3 ± 47.8	76.28 ± 2.55
Fe XVII	17.098	6.58		
O VII	18.627	6.34	36.7 ± 17.0	1.93 ± 0.89
O VIII	18.967	6.59	624.5 ± 34.8	32.58 ± 1.82
O VIII	18.973	6.59		
O VII	21.602	6.32	152.2 ± 24.5	12.23 ± 1.97
O VII	21.807	6.32	36.5 ± 19.1	2.98 ± 1.56
O VII	22.101	6.31	131.0 ± 23.9	10.75 ± 1.96
N VII	24.779	6.43	47.5 ± 19.7	3.97 ± 1.65
N VII	24.785	6.43		
C VI	33.734	6.24	114.0 ± 21.2	12.78 ± 2.38
C VI	33.740	6.24		
S XIII	35.667	6.43	43.6 ± 18.6	5.09 ± 2.17
Si XI	43.763	6.25	94.4 ± 20.9	5.31 ± 1.18
Si XII	44.019	6.44	112.6 ± 21.4	6.29 ± 1.20
Si XII	44.165	6.44	191.1 ± 23.8	10.67 ± 1.33
Si XII	45.521	6.44	34.6 ± 19.1	1.97 ± 1.09

Table 1—Continued

Ion	$\lambda_{rest}$ (Å)	$\log T$	Counts	Flux ( $10^{-5}$ cm $^{-2}$ s $^{-1}$ )
Si XII	45.691	6.44	92.7 ± 23.0	5.30 ± 1.31
Fe XVI	46.661	6.43	116.7 ± 23.6	6.77 ± 1.37
Fe XVI	46.718	6.43		
Si XI	49.222	6.24	55.6 ± 19.8	4.35 ± 1.55
Fe XVI	50.361	6.43	151.1 ± 24.4	15.81 ± 2.55
Fe XVI	50.565	6.43	30.3 ± 16.3	3.60 ± 1.94
Si X	50.524	6.15		
Si X	50.691	6.15	37.4 ± 16.6	4.99 ± 2.21
Si XI	52.298	6.24	14.9 ± 14.1	2.15 ± 2.04
Fe XVI	54.127	6.43	66.6 ± 20.5	9.06 ± 2.79
Fe XVI	54.710	6.43	117.7 ± 22.1	13.67 ± 2.57
Mg X	57.876	6.22	64.3 ± 19.6	6.05 ± 1.84
Mg X	57.920	6.22		
Fe XV	59.405	6.32	66.6 ± 19.4	6.43 ± 1.87
Fe XVI	62.872	6.42	41.3 ± 16.4	5.71 ± 2.27
Mg X	63.152	6.21	19.2 ± 13.0	2.84 ± 1.93
Mg X	63.295	6.21	37.0 ± 16.2	5.70 ± 2.49
Fe XVI	63.711	6.42	86.9 ± 18.9	16.77 ± 3.65
Fe XVI	66.249	6.42	173.2 ± 26.1	26.63 ± 4.01
Fe XVI	66.357	6.42		
Fe XV	69.682	6.32	94.3 ± 20.2	9.97 ± 2.14
Fe XV	69.941	6.32	22.3 ± 14.9	2.38 ± 1.59
Fe XV	69.987	6.32		
Fe XV	70.054	6.32		
Fe XV	73.472	6.32	45.4 ± 17.9	5.39 ± 2.13
Fe XVI	76.497	6.42	42.2 ± 18.1	5.52 ± 2.37
Ne VIII	88.082	5.96	50.2 ± 19.7	8.46 ± 3.32
Ne VIII	88.120	5.96		
Fe XVIII	93.923	6.68	303.0 ± 36.8	54.48 ± 6.62
Fe XIX	101.550	6.80	29.8 ± 20.1	6.66 ± 4.49
Fe XVIII	103.937	6.68	82.0 ± 29.1	18.86 ± 6.69
Fe XIX	108.355	6.79	133.1 ± 30.5	30.85 ± 7.07
Fe XX	121.845	6.88	82.9 ± 28.8	23.14 ± 8.04
Fe XXI	128.752	6.95	31.9 ± 19.9	13.27 ± 8.28
Fe XX	132.840	6.88	88.2 ± 32.0	36.44 ± 13.22
Fe XXIII	132.906	7.12		
Fe XXII	135.755	7.03	38.9 ± 24.1	15.73 ± 9.75
Fe IX	171.073	5.95	33.0 ± 22.6	46.92 ± 32.13
Fe X	174.534	6.04	33.9 ± 22.5	125.82 ± 83.51

Table 2. Elemental Abundances

Abundance	Stellar Corona	Stellar Photosphere <sup>a</sup>	Solar Photosphere <sup>b</sup>
Fe/Fe <sub>⊙</sub>	1.5	1.0	1.0
log [Fe/H]	−4.32	−4.50	−4.50
log [C/Fe]	0.70 <sup>+0.14</sup> <sub>−0.11</sub>	1.12	0.93
log [N/Fe]	−0.03 <sup>+0.18</sup> <sub>−0.30</sub>	(0.49)	0.33
log [O/Fe]	0.73 <sup>+0.03</sup> <sub>−0.04</sub>	1.35	1.19
log [Ne/Fe]	0.30 <sup>+0.05</sup> <sub>−0.06</sub>	(0.96)	0.43
log [Mg/Fe]	0.08 <sup>+0.12</sup> <sub>−0.06</sub>	0.08	0.10
log [Si/Fe]	0.16 <sup>+0.06</sup> <sub>−0.07</sub>	0.07	0.01
log [S/Fe]	−0.13 <sup>+0.16</sup> <sub>−0.64</sub>	(−0.22)	−0.38
log [Ni/Fe]	−1.21 <sup>+0.12</sup> <sub>−0.25</sub>	−1.33	−1.28

<sup>a</sup>From Allende Prieto et al. (2004), except for values in parentheses, which are assumed rather than directly measured (see text).

<sup>b</sup>From Asplund et al. (2009).

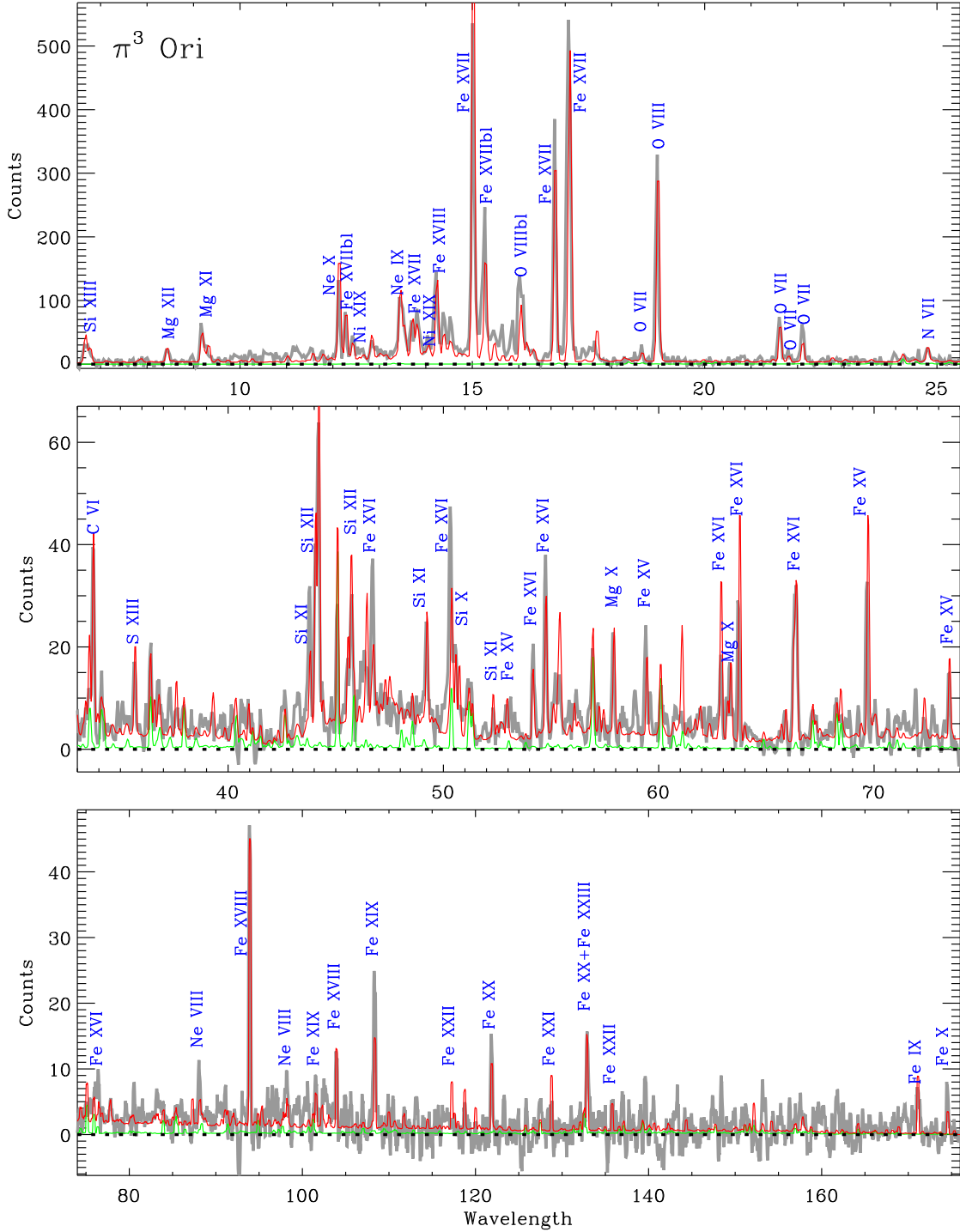


Fig. 1.— The *Chandra* LETGS spectrum of  $\pi^3$  Ori, rebinned by a factor of 3 to improve S/N. For wavelengths above 35  $\text{\AA}$ , the spectrum is also smoothed for the sake of appearance. The red line is a synthetic spectrum computed using the emission measure distribution in Figure 2, and the green lines indicate the contributions of higher spectral orders (2–5) to the model spectrum.

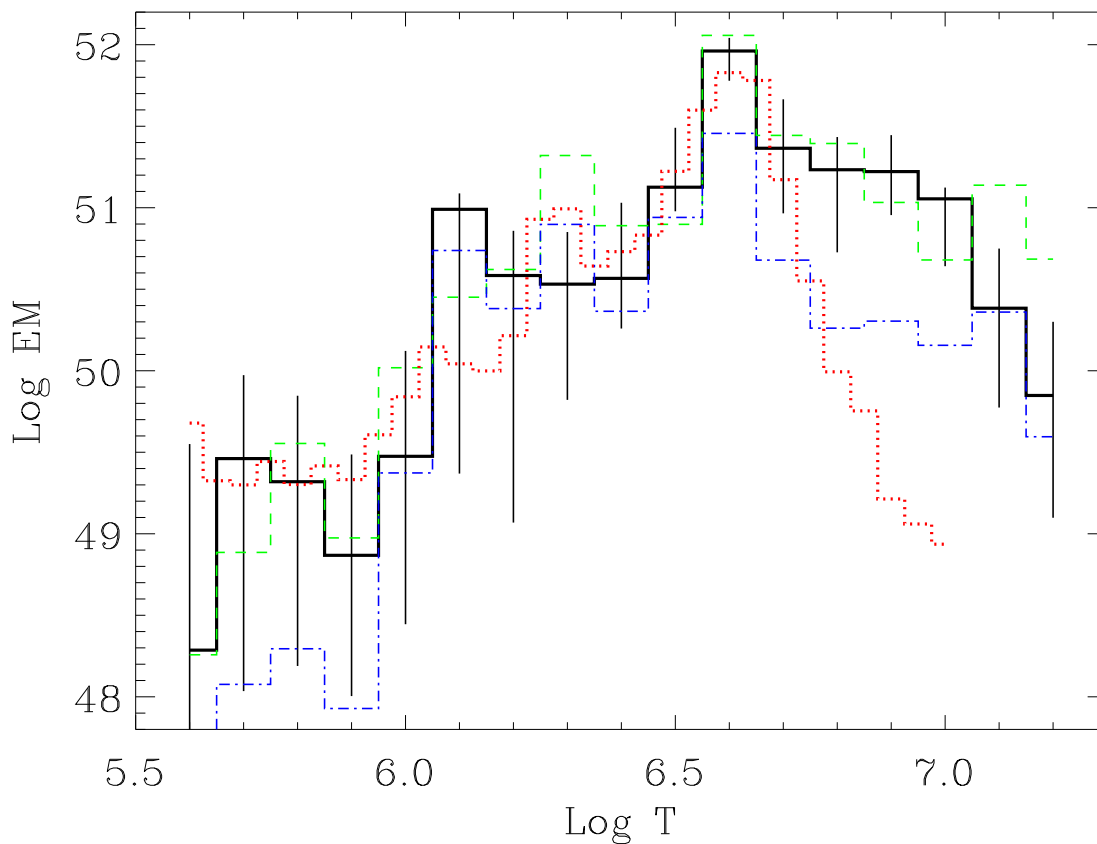


Fig. 2.— Coronal emission measure distribution derived for  $\pi^3$  Ori, with 90% confidence error bars. This is compared with distributions for  $\epsilon$  Eri (dot-dashed line) and  $\xi$  Boo A (dashed line), which were also measured from *Chandra*/LETGS data (Wood & Linsky 2006, 2010). Also shown for comparison is an average emission measure distribution for solar active regions (dotted line) studied by Warren et al. (2012). The solar distribution is normalized so that its peak matches that of  $\pi^3$  Ori.

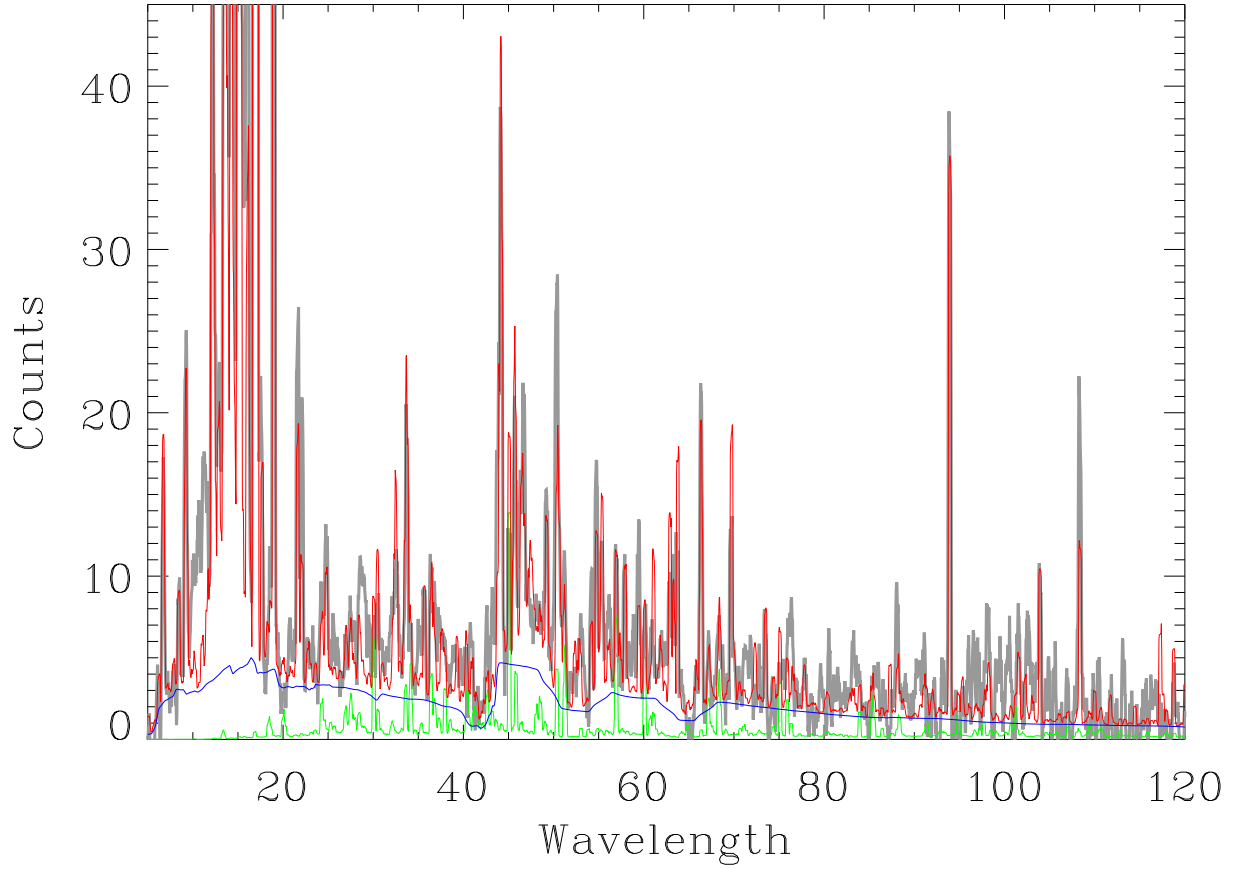


Fig. 3.— A synthetic line-plus-continuum spectrum (red line) showing the best fit to the highly smoothed *Chandra*  $\pi^3$  Ori spectrum (gray line). The continuum contribution (blue line) to the synthetic spectrum assumes an absolute Fe abundance of  $\log [\text{Fe}/\text{H}] = -4.32$ . The green line shows the contributions of higher spectral orders (2-5) to the total spectrum.

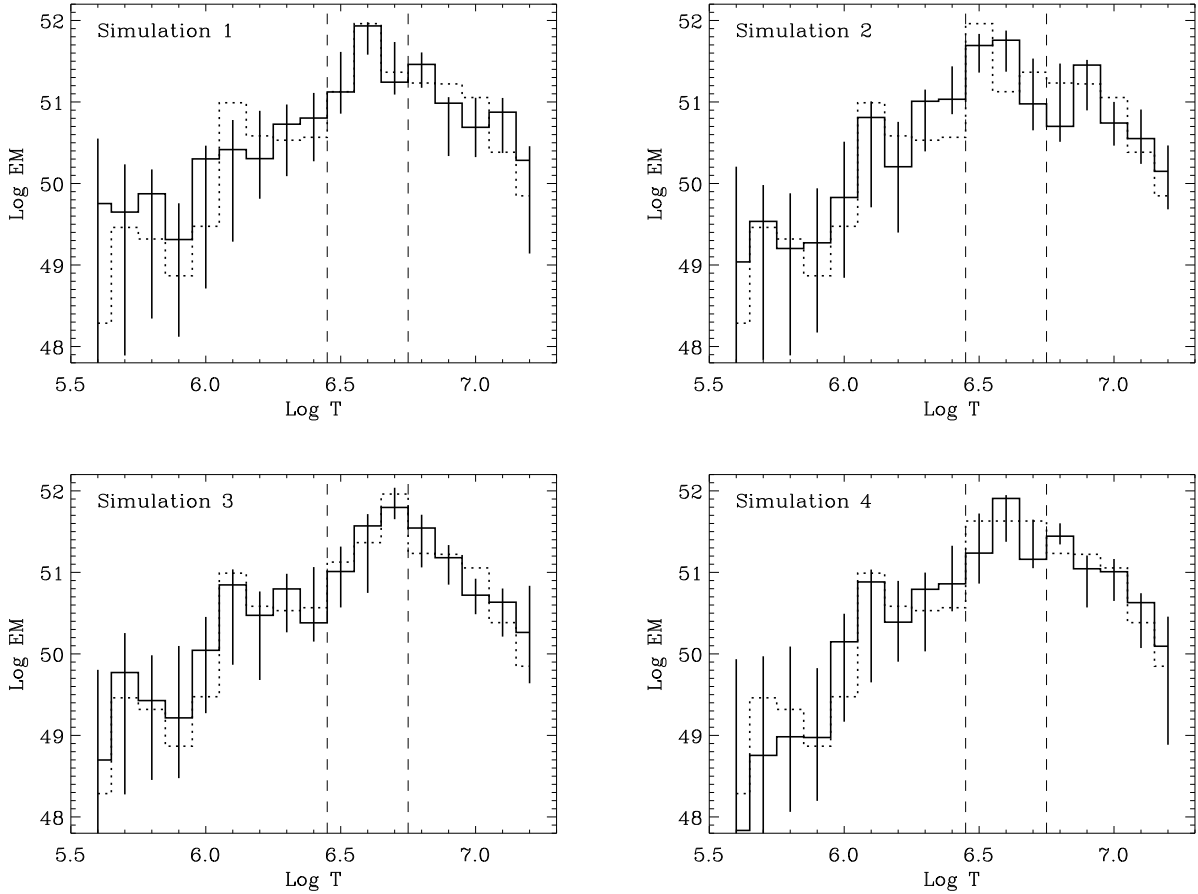


Fig. 4.— Illustration of four simulations used to assess the reliability of EM computations by PINTofALE. Dotted lines in each panels are emission measure distributions used to compute line fluxes, which are then fed into PINTofALE with the same relative uncertainties as the lines measured for  $\pi^3$  Ori. Solid lines show the resulting EM distributions, with 90% confidence intervals. In all cases, these agree reasonably well with the actual distribution. For Simulation 1, the initial seed distribution is the  $\pi^3$  Ori distribution from Fig. 2. This distribution is also used for the other three simulations, but it is modified in the  $\log T = 6.5 - 6.7$  range (marked by dashed lines) to explore PINTofALE’s ability to reproduce EM peaks at these temperatures.

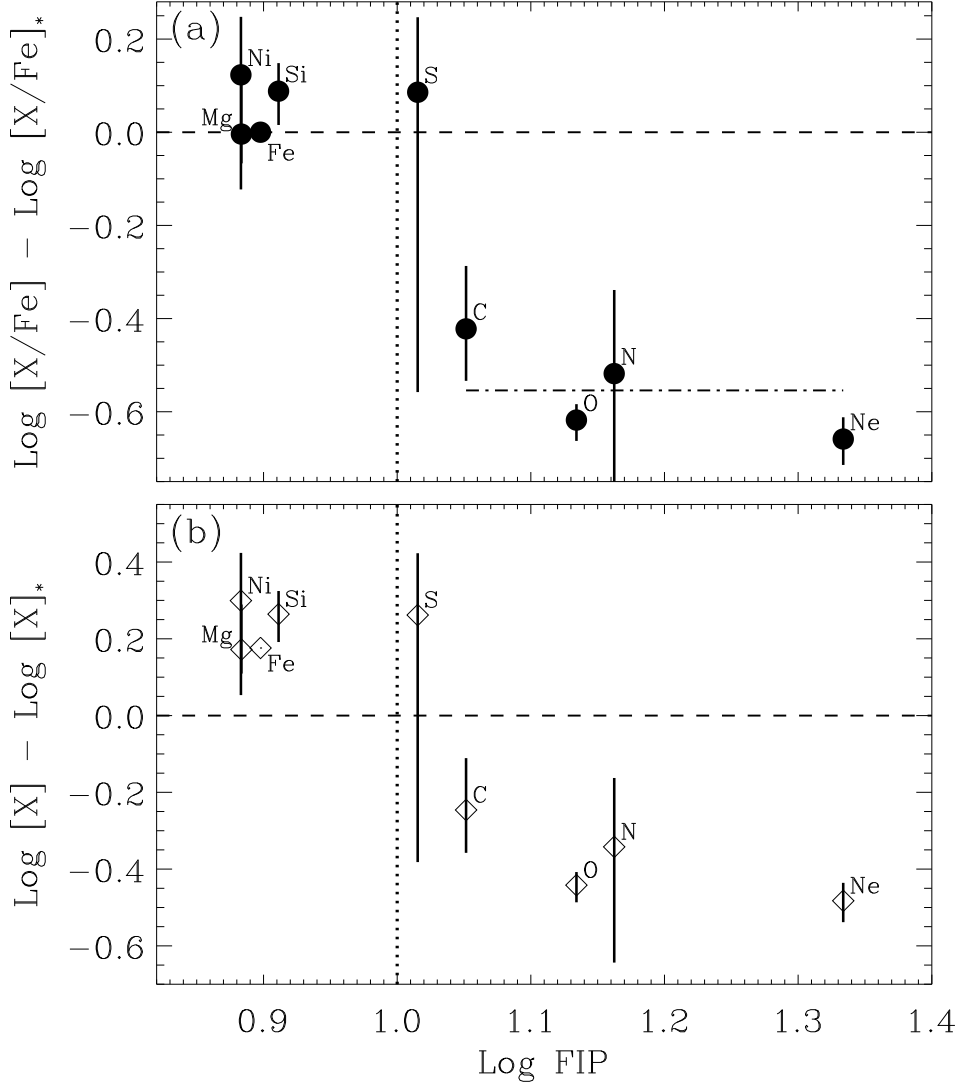


Fig. 5.— (a) The coronal abundance ratios of elements relative to Fe ( $[X/Fe]$ ) are normalized to the photospheric abundance ratios ( $[X/Fe]_*$ ) and plotted versus first ionization potential (i.e., FIP), in eV. Error bars are 90% confidence intervals derived from the emission measure analysis. The vertical dotted line separates low-FIP elements from high-FIP elements. The horizontal dot-dashed line is the average relative abundance of the four principal high-FIP elements (C, N, O, Ne), which is the  $F_{bias}$  quantity used in Fig. 6. (b) Absolute coronal abundances of  $\pi^3$  Ori relative to the photosphere, based on the  $\log [Fe/H] = -4.32$  measurement from the line-to-continuum ratio analysis (see Fig. 3).

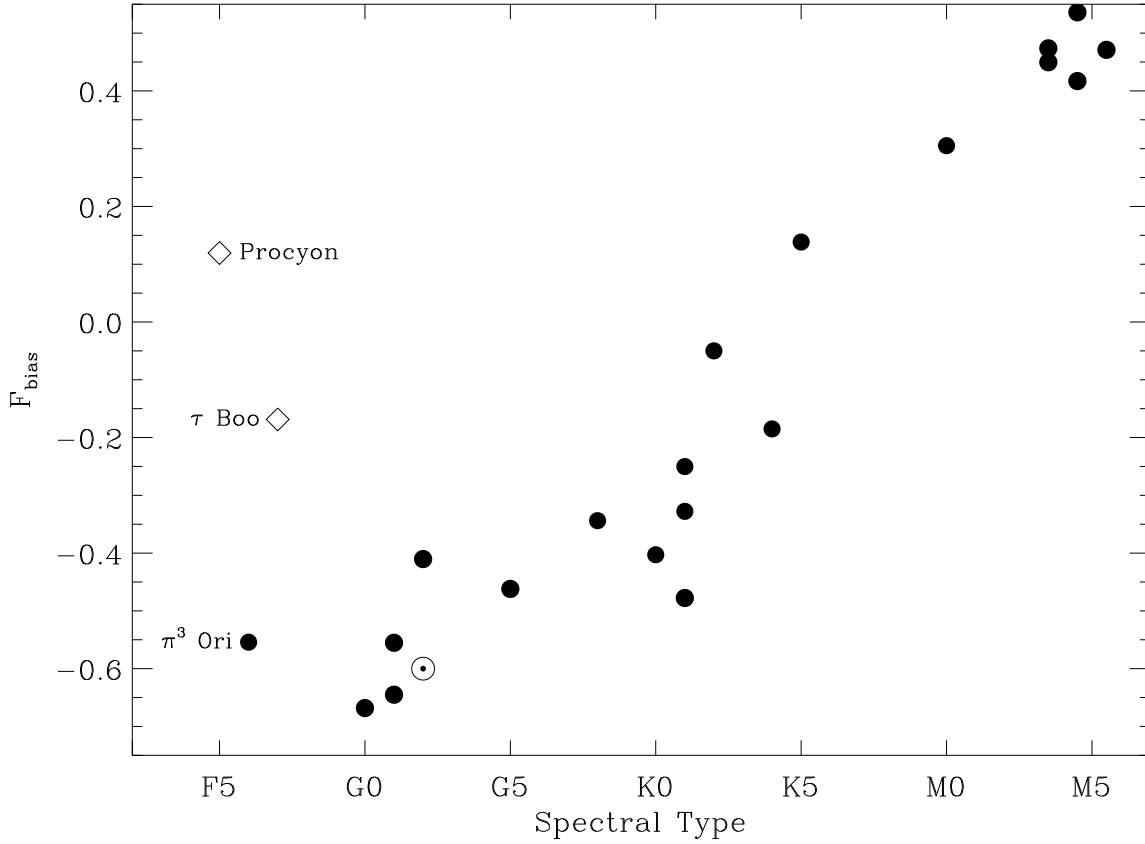


Fig. 6.— A plot of FIP bias ( $F_{bias}$ ) versus spectral type for the sample of main sequence stars from Wood et al. (2012), but with the addition of our new  $\pi^3$  Ori measurement. Measurements are also shown for two additional F stars, Procyon and  $\tau$  Boo, which are clearly inconsistent with  $\pi^3$  Ori and the general FIP-bias/spectral-type (FBST) relation.